Wind and Structures, *Vol. 23, No. 5 (2016) 465-483*
DOI: http://dx.doi.org/10.12989/was.2016.23.5.465

Pressure distribution on rectangular buildings with changes in aspect ratio and wind direction

Young Tae Lee[1], Soo Ii Boo[1], Hee Chang Lim[*1] and Kunio Misutani[2]

[1]*School of Mechanical Engineering, Pusan National University, San 30, Jangjeon-Dong, Geumjeong-Gu, Busan, 609-735, South Korea*
[2]*Department of Architecture, Tokyo Polytechnic University, Atsugi, Kanagawa, 243-0297, Japan*

(Received May 21, 2014, Revised May 28, 2016, Accepted September 20, 2016)

Abstract. This study aims to enhance the understanding of the surface pressure distribution around rectangular bodies, by considering aspects such as the suction pressure at the leading edge on the top and side faces when the body aspect ratio and wind direction are changed. We carried out wind tunnel measurements and numerical simulations of flow around a series of rectangular bodies (a cube and two rectangular bodies) that were placed in a deep turbulent boundary layer. Based on a modern numerical platform, the Navier–Stokes equations with the typical two-equation model (i.e., the standard k-ε model) were solved, and the results were compared with the wind tunnel measurement data. Regarding the turbulence model, the results of the k-ε model are in overall agreement with the experimental results, including the existing data. However, because of the blockage effects in the computational domain, the pressure recovery region is underpredicted compared to the experimental data. In addition, the k-ε model sometimes will fail to capture the exact flow features. The primary emphasis in this study is on the flow characteristics around rectangular bodies with various aspect ratios and approaching wind directions. The aspect ratio and wind direction influence the type of wake that is generated and ultimately the structural loading and pressure, and in particular, the structural excitation. The results show that the surface pressure variation is highly dependent upon the approaching wind direction, especially on the top and side faces of the cube. In addition, the transverse width has a substantial effect on the variations in surface pressure around the bodies, while the longitudinal length has less influence compared to the transverse width.

Keywords: rectangular bodies; wind direction; aspect ratio; surface pressure distribution; wind-tunnel measurement; k-ε model; Computational Fluid Dynamics

1. Introduction

The study of flow characteristics around a bluff body immersed in a turbulent boundary layer flow has long been of significant interest to researchers. Such investigations are crucial in the design and development of practical objects such as vehicles, buildings, and bridges. Over the last several decades, construction companies have employed high Reynolds number flow as a typical design parameter. Above all, the study of flow characteristics around a bluff body is now generally considered an important topic in academic circles as well as in engineering applications, and many

∗Corresponding author, Professor, E-mail: hclim@pusan.ac.kr

http://www.techno-press.org/?journal=was&subpage=8 ISSN: 1226-6116 (Print), 1598-6225 (Online)

related issues remain to be studied.

As regards flow around various types of buildings, a considerable amount of data has been generated and comparisons have been made between experimental and numerical data. One often-cited paper in this field is the wind tunnel study by Castro and Robins (1977) (hereafter denoted by CR), in which the flow around surface-mounted cubes was measured. Their paper presented the flow characteristics such as surface pressures, and mean and fluctuating velocities within a body's wake. It was the first study to demonstrate the crucial importance of modelling the appropriate atmospheric boundary layer. In addition, this paper addressed the influence of Reynolds number (Re), and found that the effects of *Re* existed for smooth upstream flow conditions (i.e., the thickness of the approaching boundary layer was much smaller than the cube height), whereas for the flow under a fully developed turbulent boundary layer, no effects of Re were found for $Re > 4000$.

As regards experimental studies, a number of papers have presented the interaction between the oncoming turbulent flow and rectangular bodies. Tieleman and Akins (1996) reported that the variations in the surface pressures at the base and sides of surface-mounted rectangular prisms were determined by the interaction between the incident turbulence and the separated shear layers. In other words, the surface pressure is a function of the small-scale turbulence that could be quantified by a modified parameter S, which is defined as the normalised spectral density of the streamwise velocity fluctuations. Furthermore, not only the value of S, but also the prism geometry (i.e., its longitudinal length-to-width (L/W) ratio) has an effect on the variations in the surface pressures at the base and sides. These results can also be seen in the study by Schofield and Logan (1990), which analysed the turbulent shear flow over surface-mounted obstacles. Their analysis concentrated on the manner in which the major features of the flow are influenced by the body geometry and the condition of incident turbulent flow. In addition, Martinuzzi and Tropea (1993) focused on the flow around surface-mounted prismatic obstacles with different spanwise dimensions, with the aim of investigating the effects of aspect ratio (i.e., width-to-height (W/H) ratio). According to the pressure measurements and vortex visualization results, the body width has a major influence on the flow characteristics in the separation, pressure recovery, and wake regions. In addition to the research on the effects of changes in aspect ratios, the effects of wind direction have also been studied by many researchers. The most notable example of studies on bodies placed at an angle to the approaching flow was the study conducted by Richards et al. (2007), who investigated the pressure distribution on the roof of a building for a range of wind directions (0°, 15°, 30°, and 45°). According to their results, both the mean and peak pressures are highly sensitive to the wind direction. For example, a change of wind direction by 30° can alter the mean static pressure coefficient from a negative value to a positive value.

As regards the computational fluid dynamics (CFD) techniques, there have been substantial changes in numerical modelling as well as hardware development, and this field continues to develop rapidly. One of the strongest merits of using a simulation is that it can provide a quick view of the full range of flow characteristics around target objects that have complex shapes at each time step and in the full domain simultaneously. For this reason, many attempts have been made to simulate the precise flow around a variety of bodies by solving the governing Navier–Stokes equations. In the early years of such research, many turbulence models were developed to solve the complicated turbulent flow around a body, some of which were compared to each other to determine their different degrees of systematic efficiency (i.e., Murakami 1993, Meroney, Leitl *et al*. 1999). It was found that the accuracy of the numerical calculation was highly dependent on the choice of the turbulence model. Most previous studies have focused on the Reynolds-averaged

Navier–Stokes (RANS) method, especially the k-ε model (e.g., Tominaga and Stathopoulos 2009). However, more comparisons and discussions are needed to judge the accuracy of the k-ε model.

Section 2, which follows, outlines the experimental techniques used, and Section 3 describes the computational techniques used. Section 4 presents an analysis of the surface pressure characteristics, as well as some findings, and discussion of the major results obtained when the aspect ratio of the bodies and the wind direction were changed. Finally, Section 5 presents the major conclusions.

2. Experimental techniques

2.1 Artificial generation of a thick turbulent boundary layer

Fig. 1 illustrates the detailed set-up inside the boundary layer wind tunnel, showing a grid, a tripping fence, roughness, and a cube model. The experiment was conducted in a closed-circuit subsonic atmospheric boundary layer wind tunnel of the Pohang University of Science and Technology in South Korea, whose working section is 0.72 m ^{height} × 0.6 m ^{width} × 6 m ^{length}, with a maximum wind speed of approximately 40 m/s. The wind tunnel is suitable for generating an artificial boundary layer, and is also equipped with a modern hot-wire anemometer (IFA100), a multi-channel pressure scanning system, and a PIV system for optical measurement of the airflow.

Thick boundary layers were generated using a technique that is often employed by wind-engineering practitioners; this technique was first devised by Cook (1978). Toothed barriers spanning the floor of the working section near its entry, followed by a square section, bi-planar mesh across the entire working section, and an appropriate rough surface after this region can be designed to yield mean-velocity profiles that are closely logarithmic over a significant portion of the working-section height, with turbulence stresses and spectra similar to those found in neutrally stable atmospheric boundary layers. There are other ways also to simulate atmospheric boundary layers (e.g., Hunt and Fernholz 1975 for an old, but still appropriate review). This particular method has the advantage of maximising the depth of the logarithmic region, but has the disadvantage of not simulating the largest-scale eddies in the upper part of the atmospheric boundary layer.

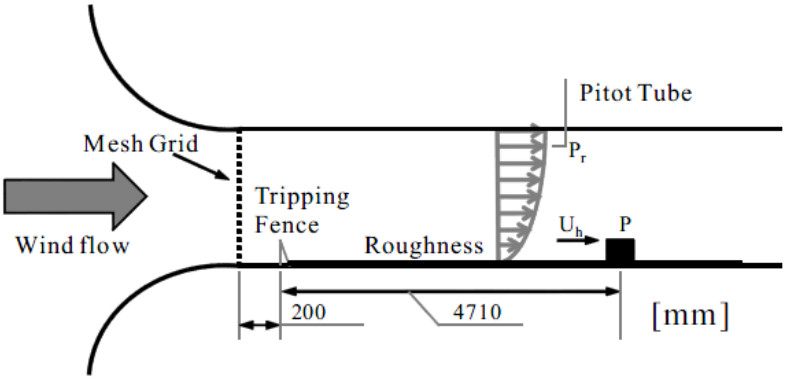

Fig. 1 The 0.6 m^{width} × 0.72 m^{height} × 6 m^{long} wind tunnel test section

As our intention was to make comparisons with the existing data such as wind tunnel and field data (e.g., for a 6 m-height cube in Silsoe, UK (Richards, Hoxey *et al*. 2001), the use of less than one-tenth of the height of the logarithmic region, thus maximising the depth of this region, was deemed the most important factor for the purposes of this study. It was also considered crucial to design the barrier wall and mix the grid geometries in tandem with the intended roughness, since any mismatch would yield unacceptably long fetches before reasonably well-developed flows are made (Lim 2009). In this case, commercially available plastic artificial grass was used to provide the surface roughness. This gave a roughness length z_0 of 0.17 mm, where z_0 is defined in the usual way via the mean velocity log law, which is expressed as

$$\frac{U}{u_*} = \frac{1}{k} ln \frac{(z-d)}{z_0} \tag{1}$$

where u_* is the friction velocity ($\sqrt{\tau/\rho}$) and d is the zero plane displacement.

To obtain the three unknowns (u_*, d, and z_0) from the mean velocity profile alone, in the present study, u_* was deduced by extrapolation of the measured turbulence shear stress ($-\overline{u'w'}$) to the surface (see Lim, Castro *et al.* 2007), and then d and z_0 were obtained from the best fit of the mean velocity data to Eq. (1). In the tunnel, the barrier wall had a height of 50 mm, with triangular cut-outs at the top; a pitch of 50 mm; and a depth of 50 mm, and the mixing grid consisted of a bi-planar grid of 10 mm bars at a pitch of 50 mm.

2.2 Building models and measurements system

Rectangular bodies with a height of 80 mm and having a smooth surface were used in the tunnel, and were equipped with 0.8 mm pressure taps at numerous salient points on the top surface, as well as on the front and side faces (see Fig. 2). Table 1 lists the rectangular models used in the study. The models were made of plexiglass and consisted of three bodies: a cube (80 mm ^{height} × 80 mm ^{width} × 80 mm ^{length} with 1:1:1 ratio) for comparing with the existing results from a reference (Lim, Thomas *et al*. 2009), and two rectangular bodies (80 mm ^{height} × 40 mm ^{width} × 80 mm ^{length} with 1:0.5:1 ratio and 80 mm ^{height} × 160 mm ^{width} × 80 mm ^{length} with 1:2:1 ratio) having dimensions in such a way that two more aspect ratios could be created for flow around the rectangular bodies by rotating them by 90° (e.g. 80 mm ^{height} × 80 mm ^{width} × 40 mm ^{length} with 1:1:0.5 ratio and 80 mm ^{height} × 80 mm ^{width} × 160 mm ^{length} with 1:1:2 ratio). Standard tube connections to a micromanometer (Furness, FC-012) allowed the measurement of mean surface pressures. Mean velocity and turbulence stress data within the boundary layers at the (subsequent) model locations and around the bodies themselves were obtained using a hot-wire anemometer (HWA). For HWA measurements, the errors caused by inadequate yaw response were minimised by using crossed-wire probes along with the standard ±45° wires (Dantec 55P61, Miniature cross-wire) and employing the effective cosine-law method to calibrate for yaw sensitivities. The probes had 1.25 mm-long platinum-plated tungsten wires with a diameter of approximately 5 μm and were driven by IFA100 (TSI) CTA bridges, with the outputs filtered to avoid aliasing. In addition, they were modified by an appropriate gain and offset to allow the best use of the analogue–digital converters (NI PCI-MIO-16E-1). Calibrations were performed against a standard pitot-static tube using the same micromanometer as was used for the (static) pressure measurements, and all analogue signals were digitized and transmitted to a desktop computer. The difference between the surface pressure p around the surface of the body and the reference pressure p_r was normalized by the dynamic pressure with free-stream velocity U_h and air density ρ

to give the surface pressure coefficient C_p, which is expressed by $C_p = (p - p_r)/0.5\rho {U_h}^2$. Specialized software ('Virtual instruments', written in National Instruments' LabVIEW) allowed online calibration and measurement of all the desired quantities. The probes were supported on traverse systems driven by the same computer. The sampling rate was typically between 2 kHz and 10 kHz, depending on the quantities being measured, with a sampling time of 60–120 s.

3. Computational techniques

3.1 Numerical methods

A schematic diagram of the computational domain with a wall-mounted bluff body is shown in Fig. 3. To make an appropriate calculation, the proper domain size is a prerequisite in the beginning state so that the cube (i.e., 80 mm $^{\text{height}}$ × 80 mm $^{\text{width}}$ × 80 mm $^{\text{length}}$) has a computational domain size of 4h $^{\text{height}}$ × 7h $^{\text{width}}$ × 14h $^{\text{length}}$ in the Cartesian coordinate system, where h is the cube height. The origin of the domain was set at the windward foot of the cube.

Table 1 Scale-down models used in the wind tunnel study

Case	H (height) [mm]	W (width) [mm]	L (length) [mm]	W/L	H:W:L
1	80	80	80	1	1:1:1
2	80	40	80	0.5	1:0.5:1
3	80	160	80	2	1:2:1
4	80	80	40	2	1:1:0.5
5	80	80	160	0.5	1:1:2

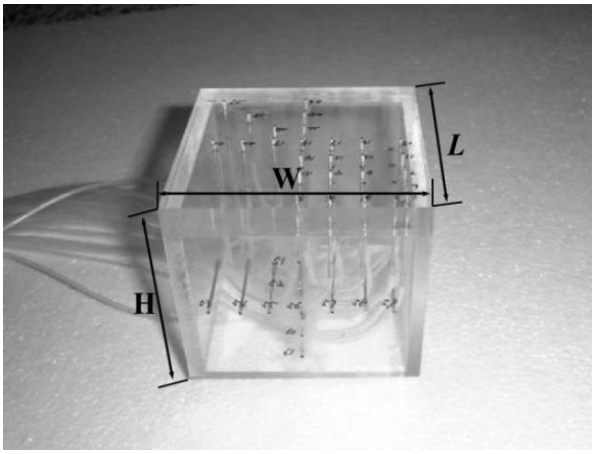

Fig. 2 A cube model (80 mm $^{\text{height}}$ × 80 mm $^{\text{width}}$ × 80 mm $^{\text{length}}$) and pressure taps

Although a gap of $3h$ both to the sides and to the roof is quite small, this computational domain is suitable for generating an appropriate turbulence boundary layer to match the real wind conditions; however, there may still be some blockage effect. In addition, the boundary conditions were set to velocity inlet (inlet condition), outflow (mass flow conservation for outlet conditions), symmetry (mirror condition for the top roof of the domain), and periodic boundary conditions (infinite perfect tiling condition on the opposite face at the same velocity), as shown in Fig. 3. To generate a practical turbulent boundary layer in the computational domain, the periodic boundary conditions would be applied in the inlet and the outlet, so that the turbulence would be developed by flow recycling, as in the Lund method (Lund, Xiaohua *et al*. 1998). When the calculation of the channel flow without any model in the computational domain is completed, the averaged mean and turbulence quantities were implanted on the inlet boundary plane of the channel flow with the rectangular body. In the case when the wind direction was changed (symbolized as ϕ, which had values of 0°, 10°, 20°, 30°, and 45°), a schematic model obtained by computational techniques was used, as shown in Fig. 4. Even though the geometry of the flow configuration is simple, the flow characteristics are essentially unpredictable, as they display multiple separations and both large- and small-scale vortex regions.

The commercial code of FLUENT was used in this calculation. In terms of the mesh size used to resolve the small-scale turbulent flow, 73, 115, and 178 nodes were used for the height, width, and length directions respectively. The first grid spacing near the wall was 0.025h and the spacing ratio was 1.1 to ensure that the value of y^+ was acceptable. Here, y^+ was defined as $y^+ = \frac{yu_*}{v}$, where y is the distance from the wall, and v is the kinematic viscosity. In this study, y^+ was approximately 45 in the standard k-ε model, and it was within the required range of 30 to 60, as suggested by Salim and Cheah (2009). For example, the inlet surface grid mesh is as shown in Fig. 5, since it requires a fine mesh resolution near the (model) wall. When the aspect ratio of the model varies, the computational domain and the number of grids must be reconstructed, as listed in Table 2. Especially, to avoid blockage effects, with increase in the angle of the wind direction, the calculation domain will also increase in proportion. For example, when the wind direction is at 45°, the calculation domain will become $4h^{\text{height}} \times 11h^{\text{width}} \times 14h^{\text{length}}$.

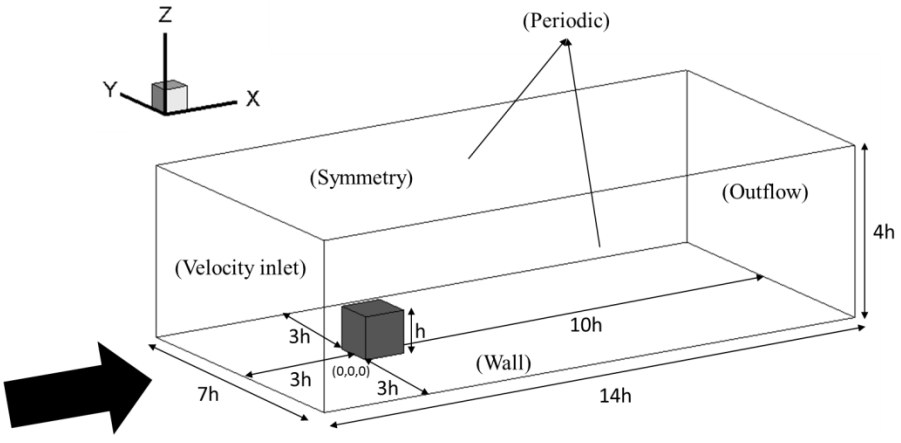

Fig. 3 Computational domain and boundary conditions

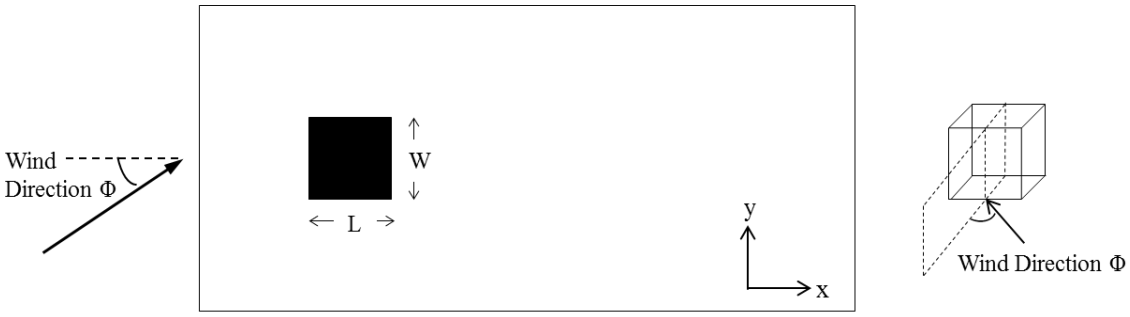

Fig. 4 Top view of a bluff body model with different wind direction angles (0°, 10°, 20°, 30°, and 45°)

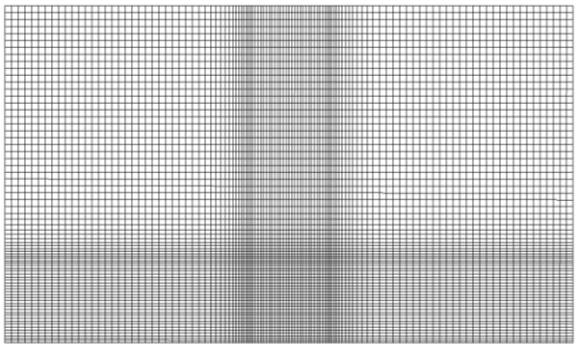

Fig. 5 Frontal view of grid mesh in the inlet condition

Table 2 Computational domains and grid nodes

Case	H:W:L	Domain	Grid nodes
1	1:1:1	4h×7h×14h	73×115×178
2	1:0.5:1	4h×6.5h×14h	73×100×178
3	1:2:1	4h×8h×14h	73×145×178
4	1:1:0.5	4h×7h×13.5h	73×115×163
5	1:1:2	4h×7h×15h	73×115×208

3.2 Governing equations and turbulence models

To describe the precise motion of fluid flow, the Navier–Stokes equations with various turbulence models must be solved, and all the boundary conditions are required to solve the equation. The RANS model was employed to render the Navier–Stokes equations tractable in order to avoid the need to directly simulate the small-scale fluctuations in turbulence.

This study implements the standard k-ε model, which is the simplest complete model of turbulence. It is a semi-empirical model, and the derivation of the model's equations relies upon empirical considerations. It is based on two separate transport equations for the turbulence kinetic energy (k) and its dissipation rate (ε). The equations are as follows

$$\frac{\partial}{\partial t}(\rho k) + \frac{\partial}{\partial x_i}(\rho k u_i) = \frac{\partial}{\partial x_j}\left[\left(\mu + \frac{\mu_t}{\sigma_k}\right)\frac{\partial k}{\partial x_j}\right] + G_k + G_b - \rho\varepsilon - Y_M + S_k \tag{2}$$

$$\frac{\partial}{\partial t}(\rho \varepsilon) + \frac{\partial}{\partial x_i}(\rho \varepsilon u_i) = \frac{\partial}{\partial x_j}\left[\left(\mu + \frac{\mu_t}{\sigma_\varepsilon}\right)\frac{\partial \varepsilon}{\partial x_j}\right] + C_{1_\varepsilon}\frac{\varepsilon}{k}\left(G_k + C_{3_\varepsilon}G_b\right) - C_{2_\varepsilon}\rho\frac{\varepsilon^2}{k} + S_\varepsilon \tag{3}$$

In these equations, G_k represents the generation of turbulence kinetic energy due to the mean velocity gradients; G_b is the generation of turbulence kinetic energy due to buoyancy; Y_M represents the contribution of the fluctuating dilatation in compressible turbulence to the overall dissipation rate; and S_k and S_ε are user-defined source terms.

In addition, μ_t is the turbulent viscosity, and is computed by combining k and ε as follows.

$$\mu_t = \rho C_\mu \frac{k^2}{\varepsilon} \tag{4}$$

In the above equations, the values of the model constants are, C_μ=0.09, C_{1_ε}= 1.44, C_{2_ε}= 1.92, σ_k= 1.0, and σ_ε= 1.3. In addition, C_{3_ε} is not specified, but is calculated according to the following relation.

$$C_{3_\varepsilon} = tanh\left|\frac{v}{u}\right| \tag{5}$$

where v is the component of the flow velocity parallel to the gravitational vector and u is the component perpendicular to the gravitational vector.

3.3 Boundary conditions

The present numerical simulation was carried out as per the conditions in the experimental study. The Reynolds number based on h (model height) and U_h (mean inlet velocity at h) was 4.6×10^4. After completing the calculation of the channel flow without any model, the averaged mean and turbulent quantities were implanted on the inlet boundary plane of the channel flow with the rectangular body. Fig. 6 compares the profiles of the inlet mean-velocity (a) and turbulence intensity (b) in the streamwise components. The results of the wind-tunnel experiment (EXP) and the numerical simulation (k-ε) were also compared with the existing results from other papers (e.g., Castro and Robins 1977 and Lim, Castro *et al*. 2007, hereafter denoted by CR and LCH). As can be seen in the vertical wind profiles, a fully developed shear flow was produced in the wind tunnel as well as in the numerical wind tunnel, which were specifically designed to be similar to the (rural) atmospheric boundary layer.

The entire domain containing the cube models, internal working section, and surface wall are shown in each figure (see Fig. 3), along with the boundary conditions for the flow. Five different boundary conditions were used in the numerical domain: inlet and outlet flow conditions for the inlet/outlet domain, periodicity for the side, symmetry for the upper wall, and wall conditions for the rest of the surface wall. The boundary layer in the domain is continuously regenerated in the channel flow, which is possible because it uses the periodicity boundary condition that combines the inlet with the outlet layer and repeatedly recirculates the flow. There are essentially two

methods for generating the necessary inflow. The first is a statistical method wherein a sequence of random numbers is generated and then filtered to yield appropriate statistical properties and spatial correlations (see Xie and Castro 2013). The second involves performing a separate 'precursor' simulation of a wind environment and sampling the inflow data directly from this simulation (see Lim, Castro *et al.* 2009). The second method has the desirable feature that the generated inflow should naturally contain physically realistic coherent structures without these having to be produced artificially; hence, this method was adopted in the present work. A similar method was used by Nozawa and Tamura (2002) in their computations of flow over a half-cube.

The velocity profile was also fitted to the power law profile, in which the exponent α was 0.14, which was dependent on the terrain roughness. The mean velocity $\bar{u}$ at the cube height was approximately 8 m/s. From the turbulence intensity profiles, it can also be seen that the high turbulence intensity (14%) was induced at a certain height (i.e., near the wall surface), and it gradually decreased in the region far away from the wall. For example, at the cube height, the turbulent intensity decreased to approximately 10.7%.

4. Results and discussion

4.1 Surface pressure distribution - cubical model (H: W: L=1:1:1)

The surface static pressure distributions along the centreline around the **1:1:1** model are shown in Fig. 7. The figure compares the numerical and experimental results for the variations in the mean static pressure coefficient $C_p = (p - p_r)/(0.5\rho {U_h}^2)$, where p_r is the mean static pressure in the upstream flow along the axial centreline of the cube. Fig. 7 also presents the existing results, i.e., the wind tunnel (WT) and field scale (FS) measurements, as a function of the measurement location x/h. Here, x = 0 corresponds to the foot of the front face of the model body, which actually depends upon the wind direction (e.g., see the solid arrowed line in the right-hand figure). It may be noted that the rest of the figures are arranged in a manner similar to the arrangement in Fig. 7, i.e., the profile at the mid-height.

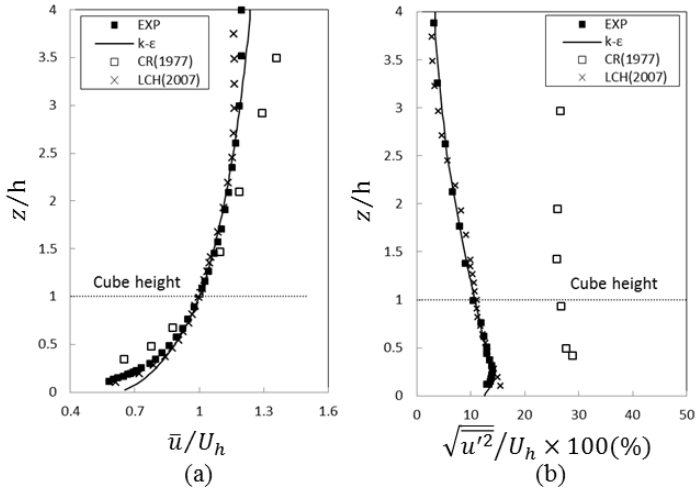

Fig. 6 (a) Mean velocity profile and (b) Turbulence intensity profile

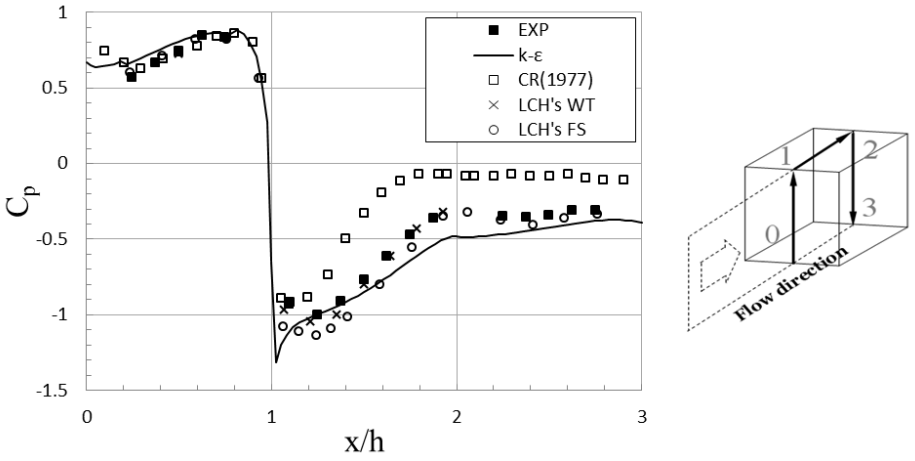

Fig. 7 Mean surface static pressure coefficient along the central section with wind normal to the face

The profiles in Fig. 7 have the expected shape in that the largest negative pressures occur just beyond the separation at the leading edge, and are followed by substantial pressure recovery on the top surface, as has been shown in numerous previous studies. It may also be noted that the experimental data agree well with the earlier field data of LCH (Lim, Castro *et al*. 2007), but are significantly different from the wind-tunnel data of CR (Castro and Robins 1977). The latter are similar to those of Murakami and Mochida (1988); they are in agreement with CR's discussion, and are undoubtedly a result of turbulence levels that are very much higher upstream, which leads to much earlier reattachment and pressure recovery on the top surface. In addition, the k-ε model data are nearly similar, except for the region just within the right-hand corner of the position x/h = 1, which has a negative peak. This seems to have been caused by the turbulence model itself. However, regardless of this peak region, there are still some variations between the experimental data and the k-ε model data. For example, in the k-ε model data, the pressure recovery is consistently underpredicted, which may be because of the blockage effects in the small-size computational domain. It is well known that the flow will be artificially accelerated by the blockage effects.

Fig. 8 shows the mean surface static pressure distribution along the mid-height of the cube. As shown in Fig. 8, the experiment data agrees well with the field measurement data of RHS (2001) (i.e., Richards, Hoxey *et al.* 2001), except for the results of CR. The k-ε model data are similar to the experiment data, but still show a significant difference just inside the right-hand corner of the position x/h = 1. The numerical data, however, show a relatively low value in the pressure recovery region (x/h = 1.4 to 3) compared to other existing works. One explanation for this might be that because of the blockage effects, the flow is artificially accelerated, so the reattachment and pressure recovery are delayed.

The reported comparison of experimental and numerical data can serve to validate a developed computational approach, which is therefore applied to analyze pressure distribution on rectangular buildings, as reported in the remaining part of this study. Therefore, the results in the current section could be seen as a precursor to the rest of the pressure profiles, as the next section discusses the pressure profiles around rectangular obstacles having the same boundary layers.

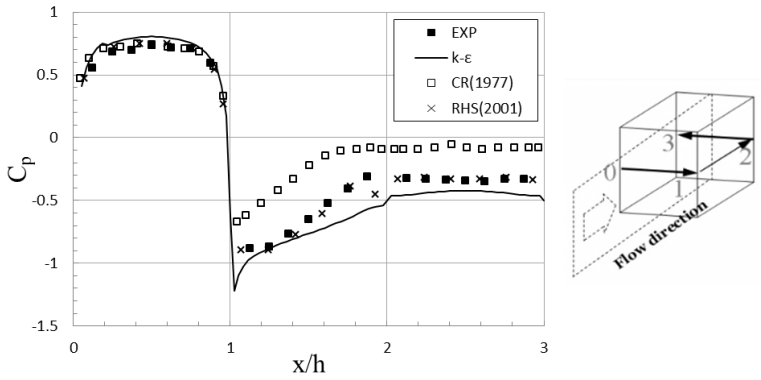

Fig. 8 Mean surface static pressure coefficient at the mid-height of the cube

4.2 Surface pressure distribution - models with different aspect ratios

The mean surface static pressure profiles along the centreline of the models using three different aspect ratios are plotted in Fig. 9. The figure shows how the surface static pressure on the top as well as on the front and rear faces varies with changes in the body width. It may be noted that several subsequent figures, i.e., Figs. 10-17, are arranged in the same manner as in Fig. 9; i.e., the pressure profiles obtained from the experiment are shown in Fig. 9(a), and those from CFD (k-ε model) are shown in Fig. 9 (b). In addition, the schematic view of the models are shown underneath the profiles, which make it easy to visualize the measurement locations around the body. In these profiles, the reason for the high suction pressure on the top surface along the centreline is obvious: the wider the shape of the body, the stronger the surface suction pressure on the top surface. It is also interesting that the front and rear faces of the body have relatively less surface pressure variations.

Another interesting phenomenon is that around the position x/h = 2, there is a small dip in the cases of 1:0.5:1 and 1:2:1; however, there is lack of data for these regions in the experimental measurements. It should also be noted that these surface pressure profiles reflect the flow features, with different aspect ratios discernible in the surface profiles of the body. The immediate implication of the data in Fig. 9 is that the variations in width, while the length and height are maintained, cause the surface pressure on the top surface to become more negative, while the front and rear faces change relatively less in response to variations in width. The solid arrow in Fig. 9 shows the direction of the pressure drop as the width changes.

Fig. 10 presents the mean surface static pressure distribution along the side face at the mid-height of the three different boxes for different transverse widths. The abscissa in Fig. 10 is normalised with the body height. Consistent with the previous figure, i.e., Fig. 9, a pressure drop with increasing width is noticeable in the negative direction. These results demonstrate that with an increase in the horizontal width, i.e., with an increase in the aspect ratio, there is a concurrent suction pressure drop on the side face. By comparison, it can be seen that the pressure difference between the cases of 1:0.5:1 and 1:1:1 was not significant in the experimental measurements. These pressure differences can be regarded as the effect of wind tunnel blockage, based on the ratio of areas of the model and the tunnel section.

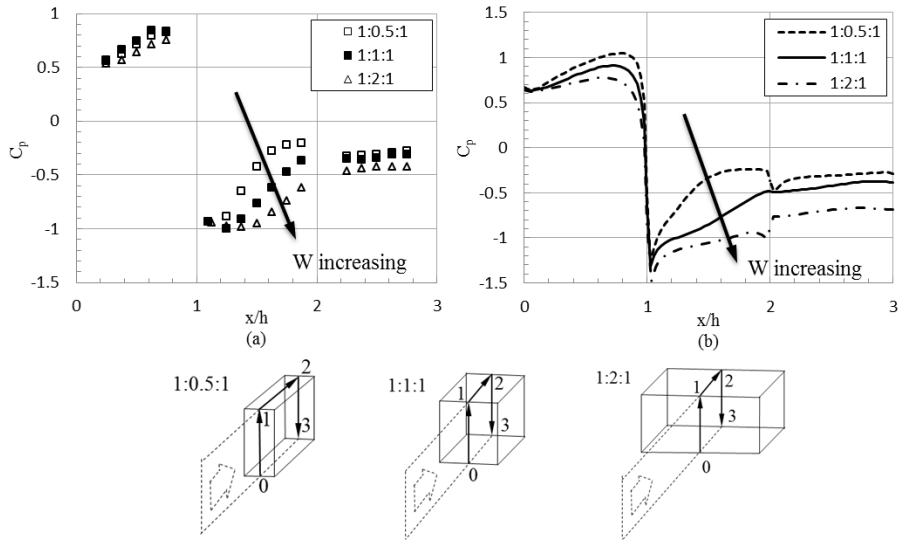

Fig. 9 Mean surface static pressure coefficient along the centreline for different transverse widths – (a) experimental results and (b) k-ε model results

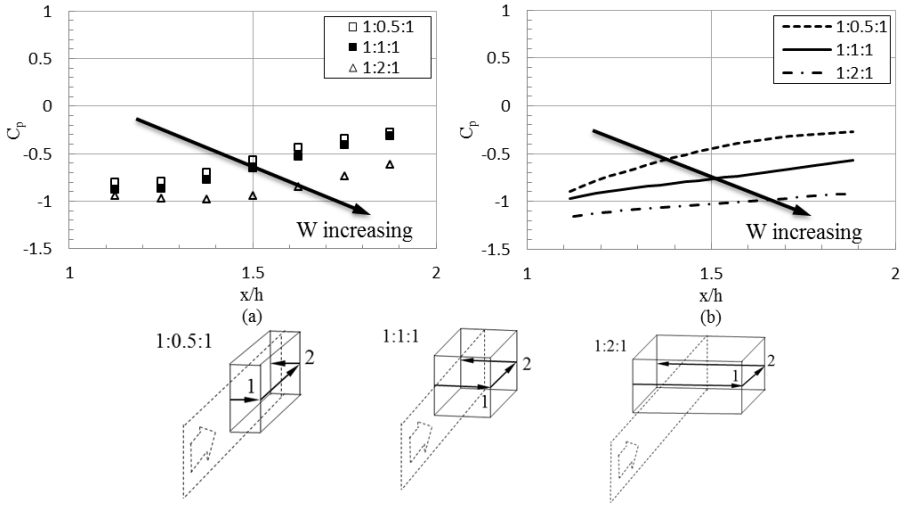

Fig. 10 Mean surface static pressure coefficient at the mid-height for different transverse widths – (a) experimental results and (b) k-ε model results

Figs. 11 and 12 show the mean surface static pressure profiles along the centreline and the mid-height of the models for different longitudinal lengths (i.e., length *l*). The different size of the longitudinal length is considered while maintaining the front face area, and the aspect ratios were 1:2:4, respectively. The flows around wall-mounted sharp-edged models usually display separation and reattachment around the body, so the pressure profiles in Figs. 11 and 12 have a similar shape

as shown in the above results. In Figs. 11 and 12, the pressure profiles seem to show a similar trend, and it may be noted that the overall distributions of the surface pressure are in good agreement. However, there are still some variations between each case. We may thus draw the conclusion that compared to the significant transverse width effects seen in Figs. 9 and 10, the longitudinal length of the body has less influence (but it exists) on the surface pressure around rectangular bodies.

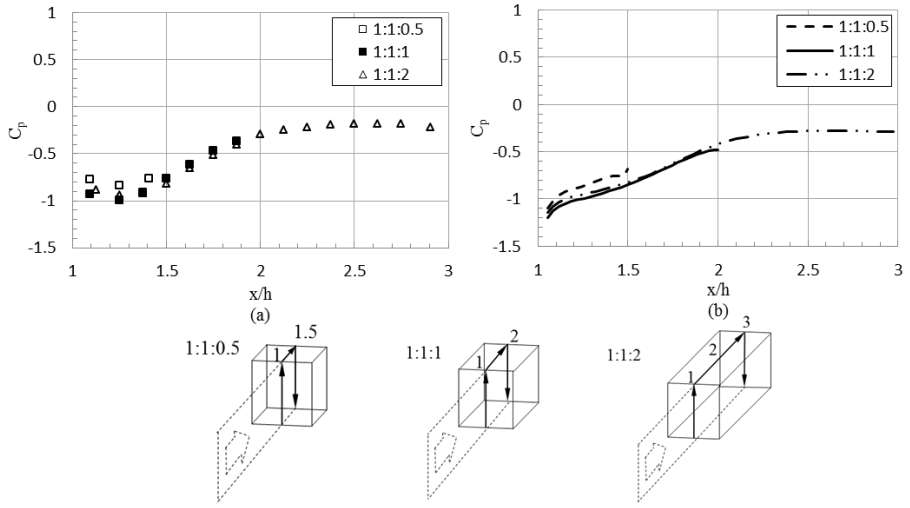

Fig. 11 Mean surface static pressure coefficient along the centreline for different longitudinal lengths – (a) experimental results and (b) k-ε model results

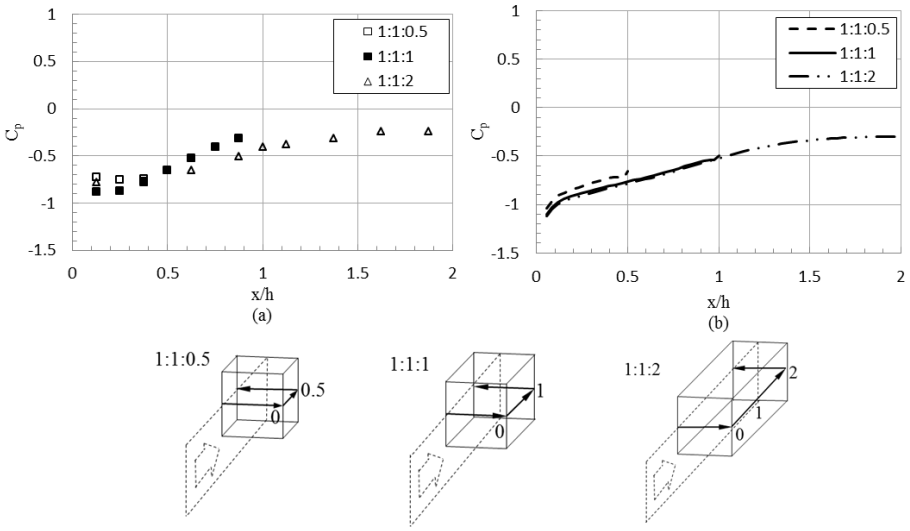

Fig. 12 Mean surface static pressure coefficients at the mid-height for different longitudinal lengths – (a) experimental results and (b) k-ε model results

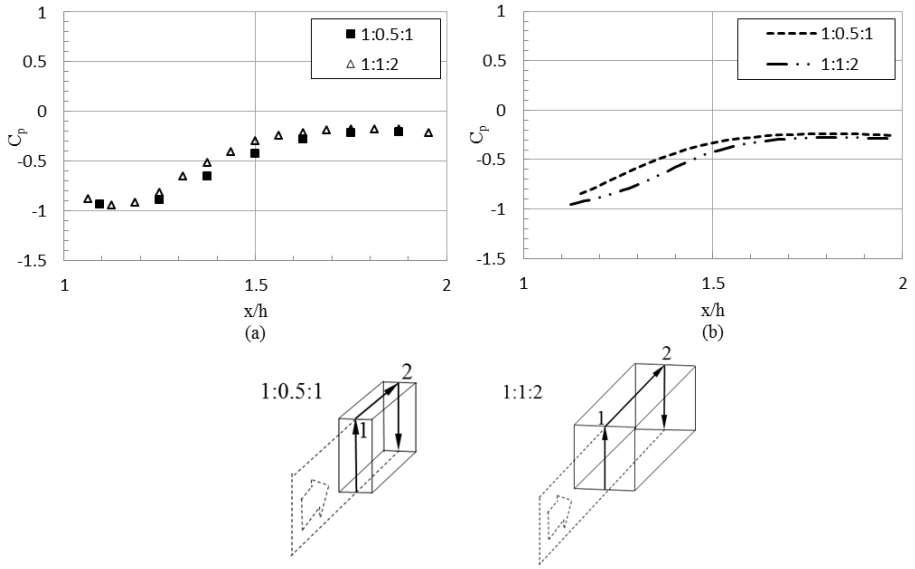

Fig. 13 Mean surface static pressure coefficient along the centreline with change in width and length at the same time, but with the ratio W/L = 0.5 unchanged – (a) experimental results and (b) k-ε model results

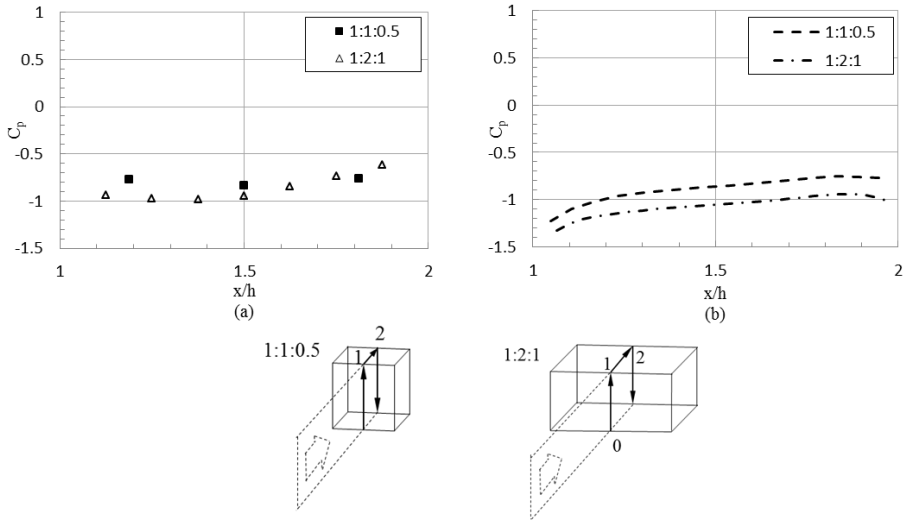

Fig. 14 Mean surface static pressure coefficient along the centreline with change in width and length at the same time, but with the ratio W/L = 2 unchanged – (a) experimental results and (b) k-ε model results

Figs. 13 and 14 present the pressure coefficient comparisons for the cases when both the length and width of the body are changed, but the ratio of width over length (i.e., W/L) is the same. Fig. 13 shows the pressure distribution on the top surface when the W/L ratio is 0.5, whereas Fig. 14 shows the distribution when the W/L ratio is 2. In Figs 13 and 14, although there is an obvious gap

between the cases 1:0.5:1 and 1:1:2, and between the cases 1:1:0.5 and 1:2:1, the trend of the variation is generally similar. Even though the length and width of the rectangular body have changed, with the width over length ratio unchanged, the characteristics of the static surface pressure profiles, at least along the centreline, remain unchanged. If there is any change in the profiles, it is because of a little scatter. We might regard this scatter of pressure differences as the wind tunnel blockage effect. Furthermore, a larger body is far more prone to the blockage effect.

4.3 Surface pressure distribution – models with different wind directions

Richards, Hoxey *et al.* (2007) have created a 1:40 scale wind tunnel model of the Silsoe 6 m Cube. In their research, the effects of wind direction are shown by altering the angle in 15° steps (0°, 15°, 30°, and 45°). Their results are presented in Figs. 15(a) and 16(a), and can be compared with the CFD data in Figs. 15(b) and 16(b). In the present study, to observe the effect of wind direction on the pressure variations around the cube (80 mm $^{\text{height}}$ × 80 mm $^{\text{width}}$ × 80 mm $^{\text{length}}$, a 1:75 scale-down model), it is rotated by 0°, 10°, 20°, 30°, and 45°, which represent the salient wind directions in the tunnel measurements. The results are given below.

The mean surface static pressure profiles along the centreline of the models with different wind directions are plotted in Fig. 15. Fig. 15 shows how the surface pressure along the centreline varies with change in the wind direction. It may be noted that Fig. 16, which follows, is arranged in a manner similar to Fig. 15; i.e., the experimental results of Richards, Hoxey *et al*. (2007) are shown on the left, and the CFD results (k-e) on the right. Even when the wind direction is changed, the static pressure coefficient is still a function of the measurement location x/h. By comparing the two figures, i.e., Figs 15 and 16, it can be seen that the data from CFD results are generally in good agreement with the earlier wind tunnel data of Richards, Hoxey *et al.* (2007). It can also be seen that these surface pressure profiles reflect the flow features with different wind directions. As shown in Fig. 15, the profiles have the same expected shape as before, in spite of different wind directions, in that the largest negative pressures still occur just beyond the separation at the leading edge, and are followed by substantial pressure recovery on the top surface.

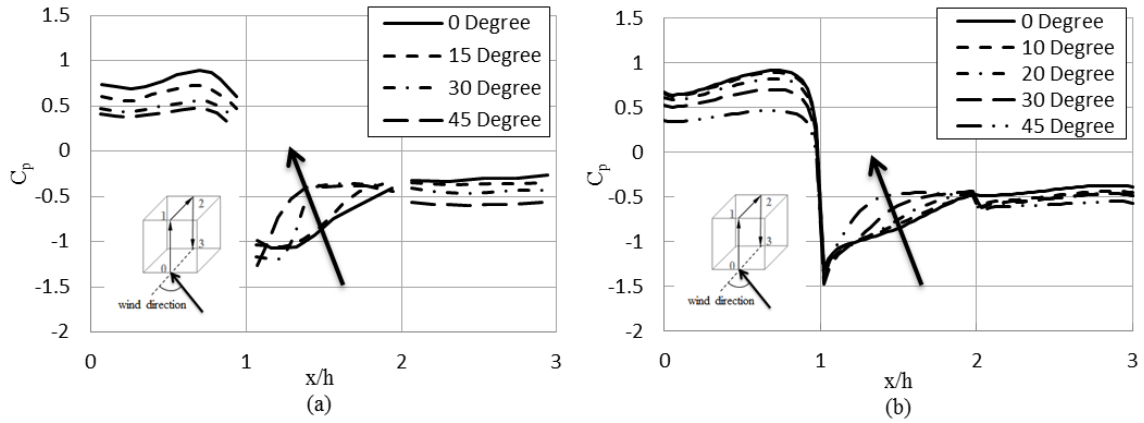

Fig. 15 Mean surface static pressure coefficient along the centreline for different wind directions – (a) experimental results of Richards, Hoxey *et al*. (2007) and (b) k-ε model results

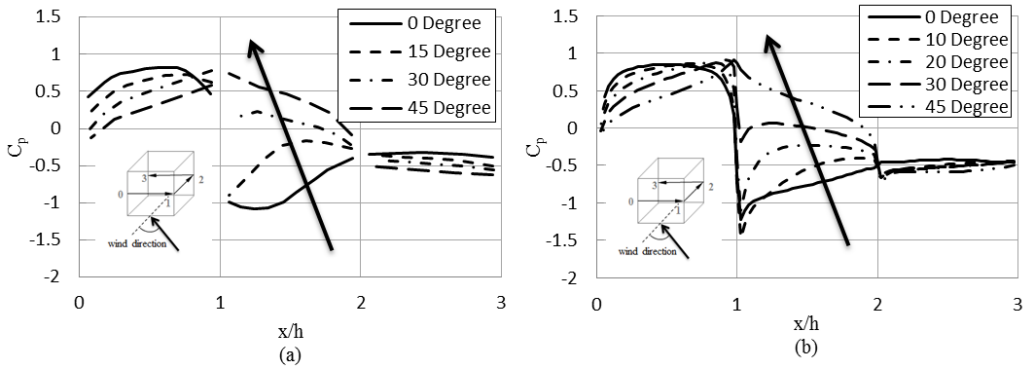

Fig. 16 Mean surface static pressure coefficient at the mid-height for different wind directions – (a) experimental results of Richards, Hoxey *et al*. (2007) and (b) k-ε model results

Although effects of changes in the angle of wind direction in Richard's experiment differ from the results of this study's numerical simulation, the same trend can be seen, in that the greater the angle of the wind direction, the weaker the surface suction pressure on the top face. The surface suction pressure on the rear face, however, shows the opposite trend. In addition, the positive pressure on the front face also becomes weaker as the angle of the wind direction increases. In addition, the amplitude of the surface pressure variation on the rear face is less than that on the front and top faces.

Fig. 16 shows the mean surface static pressure at the mid-height of the cube for different wind directions. Compared to the results in Fig. 15, the surface static pressure coefficient profiles in Fig. 16 display greater changes, particularly on the side face for the positions x/h = 1 to 2. Both the experimental results of Richards in Fig. 16(a) and CFD results in Fig. 16(b) indicate that the surface pressures on these walls are highly sensitive to the wind direction. For example, for the side face, a change of wind direction by 30° can cause a considerable change in the pressure coefficient, and can even change the pressure coefficient from a negative value to a positive value.

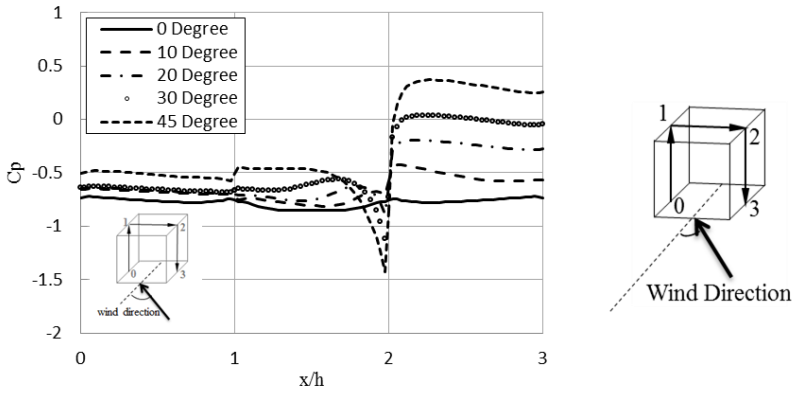

Fig. 17 Mean surface static pressure coefficient along the transverse centreline for different wind directions

Fig. 17 presents the mean surface static pressure along the transverse centreline of the cube for different wind directions, but the data from Richards, Hoxey *et al*. (2007) is not presented for comparison. In Fig. 17, it can be seen that when the wind direction is 0°, the profile is symmetrical. In addition, the largest negative pressures occurs in the middle of the top surface, and is followed by gradual pressure recovery that is associated with the separation and reattachment range on the top and side surfaces. However, once the wind direction changes, the profiles show some asymmetry, and the largest suction pressure position also changes, as shown in Fig. 17. When the wind direction changes from 10° to 45°, the surface suction pressure becomes gradually weaker. In particular, at the positions x/h = 2 to 3, the surface pressure even changes from negative pressure to positive pressure when the wind direction changes, until it reaches 45°.

5. Conclusions

To understand the surface pressure distribution around rectangular bodies with different aspect ratios and wind directions, we conducted wind tunnel measurements and numerical simulation (in the case of the turbulence model, we used the standard k-ε model) of flow around a series of rectangular bodies placed in a deep turbulent boundary layer. According to the results of the velocity and pressure measurements, substantial changes were observed in the flow and pressure characteristics around the rectangular bodies. In this study, the results of the mean static pressure coefficient were compared for various aspect ratios and wind directions. Ultimately, the numerical k-ε model results were compared with the wind tunnel experimental data and the existing field data.

We mainly focused on the effects of various aspect ratios and approaching wind directions on the flow characteristics around rectangular bodies. We summarize our major contribution as follows. First, for flows and wind loads around rectangular obstacles, the aspect ratio and wind direction are important, and can be used for the design and deployment of neighbouring buildings and structures. Second, despite the lack of wind tunnel data, new mean flow data for a variety of model cases have been generated. Third, this paper includes much more reasonable and improved flow quantities based on the numerical calculation than earlier ones. Finally, we observed that the aspect ratio of a rectangular body and the wind direction have a substantial effect on the surface pressure around the body, a finding that has never before been reported in the existing papers.

Although more comparisons are needed to arrive at more definitive conclusions, this study is able to contribute with the following findings.

(1) The CFD (k-ε model) results are in overall agreement with the experimental results, including the existing data. However, because of the blockage effects in the computational domain, the numerical data underpredicts the pressure recovery as compared to the experimental data. In addition, the k-ε model sometimes fails to capture the exact flow features in some special regions; for example, a relatively higher negative sharp peak (strong suction) close to the leading edge compared to the other existing works.

(2) The turbulent flow around the wall-mounted bluff body separates from the front edge of the body, and then reattaches on the top and side faces. Regarding the pressure distribution, the largest negative pressures occur just beyond the separation region, and are followed by substantial pressure recovery on the top and side faces. In addition, a higher upstream turbulence level will lead to much earlier reattachment and pressure recovery, as well as higher static pressure coefficient.

(3) When the wind direction towards a bluff body changes, the variation in the surface pressure on the body is highly sensitive to the wind direction, especially on the top face and the side face of a cubical body. Sometimes, a change of wind direction by 30° can even change the pressure coefficient from a negative value to a positive value.
(4) When the aspect ratio of a rectangular body changes, the transverse width has a substantial effect on the surface pressure around the body; for example, the wider the geometry of body becomes, the stronger the surface suction pressure on the top and side faces will be. In addition, compared to the substantial effects of the body transverse width, the longitudinal length shows less influence (but it exists) on the surface pressure variation.

Acknowledgments

This work was supported by "Human Resources Program in Energy Technology" of the Korea Institute of Energy Technology Evaluation and Planning (KETEP), granted financial resource from the Ministry of Trade, Industry & Energy, Republic of Korea (No. 20164030201230). In addition, this work was supported by the National Research Foundation of Korea (NRF) grant funded by the Korea government (MSIP) (No. 2016R1A2B1013820). This work was also supported by the China-Korea International Collaborative work (Project ID: SLDRCE15-04).

References

Castro, I.P. and Robins, A.G. (1977), "The flow around a surface mounted cube in uniform and turbulent streams", *J. Fluid Mech.*, **79**(2), 307-335.
Cook, N.J. (1978), "Wind tunnel simulation of the adiabatic atmospheric boundary layer by roughness, barrier and mixing device methods", *J. Wind Eng. Ind. Aerod.*, **3**(2-3), 157-176.
ESDU (1985), "Characteristics of atmospheric turbulence near the ground. part ii: single point data for strong winds (neutral atmosphere)", *In Engineering Sciences Data Unit*.
Hunt, J.C.R. and Fernholz, H. (1975), "Wind-tunnel simulation of the atmospheric boundary layer: a report on Euromech 50", *J Fluid Mech.*, **70**(3), 543-559.
Jochen, F. and Dominic, V.T. (2008), "Hybrid LES/RANS methods for the simulation of turbulent flows", *Prog. Aerosp. Sci.*, **44**(5), 349-377.
Lim, H.C. (2007), "Generation of a turbulent boundary layer using LES", *Trans of the KSME (B)*, **31**(8), 680-687.
Lim, H.C. (2009), "Wind flow around rectangular obstacles with aspect ratio", *Wind Struct.*, **12**(4), 299-312.
Lim, H.C., Castro, I.P. and Hoxey, R.P. (2007), "Bluff bodies in deep turbulent boundary layers:Reynolds-number issues", *J. Fluid Mech.*, **571**, 97-118.
Lim, H.C., Thomas, T.G. and Castro, I.P. (2009), "Flow around a cube in a turbulent boundary layer: LES and experiment", *J. Wind Eng. Ind. Aerod.*, **97**(2), 96-109.
Lund, T.S., Xiaohua, W. and Squires, K.D. (1998), "Generation of turbulent inflow data for Spatially-Developing boundary layer simulations", *J. Comput. Phys.*, **140**(2), 233-258.
Martinuzzi, R. and Tropea, C. (1993), "The flow around surface-mounted, prismatic obstacles placed in a fully developed channel flow", *J. Fluid Eng. - ASME*, **115**(1), 85-92.
Meroney, R.N., Leitl, B.M., Rafailidis, S. and Schatzmann, M. (1999), "Wind tunnel and numerical modeling of flow and dispersion about several building shapes", *J. Wind Eng. Ind. Aerod.*, **81**(1-3), 333-345.
Murakami, S. (1993), "Comparison of various turbulence models applied to a bluff body", *J. Wind Eng. Ind.*

Aerod., **46-47**, 21-36.
Murakami, S. and Mochida, A. (1988), "3D numerical simulation of airflow around a cubic model by means of k-E model", *J. Wind Eng. Ind. Aerod.*, **31**(2-3), 283-303.
Nozawa, K. and Tamura, T. (2002), "Large eddy simulation of the flow around a low-rise building immersed in a rough-wall turbulent boundary layer", *J. Wind Eng. Ind. Aerod.*, **90**(10), 1151-1162.
Richards, P.J., Hoxey, R.P. and Short, L.J. (2001), "Wind pressure on a 6 m cube", *J. Wind Eng. Ind. Aerod.*, **89**(14-15), 1553-1564.
Richards, P.J., Hoxey, R.P., Connell, B.D. and Lander, D.P. (2007), "Wind-tunnel modelling of the Silsoe cube", *J. Wind Eng. Ind. Aerod.*, **95**(9-11), 1384-1399.
Salim, S.M. and Cheah, S.C. (2009), "Wall y^+ strategy for dealing with wall-bounded turbulent flows", *Proceedings of the International Multi-Conference of Engineers and Computer Scientists*, Hong Kong.
Schofield, W. and Logan, E. (1990), "Turbulent shear flow over surface-mounted obstacles", *J. Fluid Eng. - ASME*, **112**(4), 376-385.
Shur, M. L., Spalart, P.R., Strelets, M.K. and Travin, A.K. (2008), "A hybrid RANS-LES approach with delayed-DES and wall-modelled LES capabilities", *J. Heat Fluid Fl.*, **29**(6), 1638-1649.
Simiu, E. and Scanlan, R.H. (1996), *Wind effects on Structures-Fundamentals and Applications to Design*, (3rd Ed.). Wiley, New York, USA.
Tieleman, H.W. and Akins, R.E. (1996), "The effect of incident turbulence on the surface pressures of surface-mounted prisms", *J Fluid. Struct.*, **10**(4), 367-393.
Tominaga, Y. and Stathopoulos, T. (2009), "Numerical simulation of dispersion around an isolated cubic building: comparison of various types of k-ε models", *Atmos. Environ.*, **43**(20), 3200-3210.
Xie, Z.T. and Castro, I.P. (2008), "Efficient generation of inflow conditions for large-eddy simulations of street-scale flows", *Flow Turbul. Combus.*, **81**(3), 449-470.

CC